Understanding Effects of Ni Particle Size on Steam Methane Reforming Activity by Combined Experimental and Theoretical Analysis

Yalan Wang[1], Hongmin Wang[1], Anh Hoang Dam[1], Ling Xiao[2], Yanying Qi[1], Juntian Niu[1], Jia Yang[1], Yi-An Zhu[2,*], Anders Holmen[1], De Chen[1,*]

[1] *Department of Chemical Engineering, Norwegian University of Science and Technology (NTNU), N-7491 Trondheim, Norway*

[2] *State Key Laboratory of Chemical Engineering, East China University of Science and Technology, Shanghai, 200237, China*

To whom correspondence should be addressed: yanzhu@ecust.edu.cn and de.chen@ntnu.no

Abstract

Fundamental understanding of the size dependent activity is essential to harness powers of the nanocatalysts. Here we report an experimental and theoretical study of the Ni particle size effect on activity of steam methane reforming (SMR) to achieve a better understanding of the size dependence of kinetic behavior at an atomic level. A kinetic study illustrated the higher forward methane turnover frequency on the smaller sized Ni particles. The size dependent activity was well reproduced by microkinetic modeling on a truncated octahedron model with the kinetic parameters estimated by the improved unity bond index-quadratic exponential potential (UBI-QEP) and the Brønsted-Evans-Polanyi (BEP) relationship. Microkinetic modeling suggested that the size-dependent activity of Ni catalysts is associated with surface-dependent activity. Much higher activity of Ni(211) than Ni(111) and Ni(100) accompanied by decreased Ni(211) surface fraction results in reduced Ni activity as particle size increasing. The activity of Ni(111) is limited by high free energy barrier, while that of Ni(100) is limited by surface C* and CH* blockage. This work offers a feasible approach to gain insight into size-dependent activity and to aid rational catalyst design that preparing extremely small Ni particles ($\leqslant$ 6 nm) might be a good strategy for SMR.

Keywords: Steam methane reforming; Ni catalysts; Size-dependent activity; Microkinetic modeling; Surface-dependent activity; mechanism research

1. Introduction

The production of hydrogen has attracted increasing attention due to its importance in the chemical industry, as well as application in future energy infrastructures performed as a potential energy-carrier [1]. Currently, the main process for hydrogen production is steam methane reforming (SMR), which has long been of interest for researchers. Moreover, steam methane reforming acts as a source of synthesis gas, which can be subsequently utilized for higher value chemicals production. Selection of proper SMR catalysts to achieve high hydrogen and synthesis gas production is of great significance. To date, many attempts have been made to investigate SMR catalytic activity across various transition metal catalysts via both experimental [2-11] and theoretical studies [11-13]. Most studies demonstrate a generally accepted activity tendency at atmosphere pressure with temperature in the range of 623-1173 K: Ru, Rh > Ni, Ir > Pt, Pd > Co, Fe, except for Wei and Iglesia's work, which reported activity trend as Pt > Ir > Rh > Ru, Ni at 873 K [5-10]. Despite the controversy over activity of different metals, Ni is employed as a commercial and mature industrial catalyst for SMR because of its low cost and its abundance [14]. However, the limited activity is one of major challenges of Ni-based catalysts [15] for pre-reforming of natural gas and other compounds. Finding effective methods to increase Ni activity and improve the economic efficiency of SMR is essential for both academic research and industrial application.

Particle size is considered as an important parameter to influence the activity of SMR catalysts [16, 17]. For instance, with decreased particle size, increased activity of SMR catalysts [9, 11, 18] and reduced coke formation [19-21] have been reported in literature. Smaller particle size leads to a larger surface-to-volume ratio and hence improved catalytic activity [16, 22, 23]. In addition, smaller particles display larger fractions of low-coordination surface sites (such as steps, kinks and defects) [24, 25], which are expected as the most active sites for SMR [11]. Higher turnover rates are therefore observed in smaller particles than larger particles. Although many efforts have been devoted to gain a better understanding of size-dependent activity towards SMR, the quantitative analysis of different surface contribution to total activity and the direct evidence to reveal

origin of Ni particle size effect remains a challenge. Understanding these would be undoubtedly valuable for rational catalyst design.

Combination of experiments and theoretical modeling provides the possibility to help understand the real reaction and gain insight into size-dependent activity. According to the work of Green et al. [1], one Ni particle can be simulated by using a truncated octahedron model, which consists of Ni(111) and Ni(100) surfaces. Boundaries between these surfaces are treated as Ni(211) surface. The model predicted three surfaces fractions versus particle size fit full Wulff construction data [26] very well with particle size in the range of 0 to 10 nm. Towards each surface, microkinetic modeling offers the opportunity to probe their activity, which takes into account not only the energy but also coverage information [1, 27-29], therefore gives a more accurate estimation of activity than only barrier analysis. Input parameters of microkinetic model are normally calculated either by density functional theory (DFT) calculations [30-32] or by semi-empirical approaches, such as unity bond index-quadratic exponential potential (UBI-QEP) [33-35], linear scaling relationship [36-38], group additivity [39-41], Brønsted-Evans-Polanyi (BEP) relationship [42-44] and so on. DFT calculations display a relatively high accuracy but it is time-consuming and expensive [45, 46]. In contrast, semi-empirical approaches are time-saving and much less expensive, while low accuracy is a major problem occurred. In this situation, we have proposed a hybrid semi-empirical approach (improved UBI-QEP + BEP), which exhibits a reasonable accuracy with respect to DFT but reduces radically the computational costs [47], where the UBI-QEP model was radically improved and BEP-relationships on C-H, C-O, C-C, O-H bond cleavage and formation were obtained based on a large set of DFT data on different surfaces of transition metals. The approach is applied here for rapidly generating surface energetics.

In the present study, hydrotalcite-drived Ni catalysts are prepared with different particle size to investigate the size-dependent activity of SMR. Meanwhile, truncated octahedron model is utilized to simulate the similar size Ni particles, with microkinetic modeling to predict their activity. The microkinetic modeling is performed

on CatMAP (Catalysis Microkinetic Analysis Package), a software package to describe catalytic trends via descriptor-based microkinetic mapping [48-50]. At first, SMR is simulated on the most close-packed surfaces of Ru, Rh, Ni, Pt, Pd, Co, Fe and Cu to generate the volcano plot, with the combined UBI-QEP method and BEP relationships to estimate surface energetics. After preliminary microkinetic modeling, the rate-determining steps (RDSs) can be obtained. Then DFT computations are adopted to calculate the activation energies of RDSs to acquire a refined microkinetic model, which is employed as a benchmark to predict catalyst activity over Ni(211) and Ni(100) surfaces, by using C- and O-metal binding energies as descriptors. The particle size effect is subsequently analyzed and explained from theoretical points of view. This work provides a possible approach to gain insight into particle size effect on activity and to contribute to rational catalyst design.

2. Methods

2.1 Experimental methods

Hydrotalcite like materials containing 12wt%Ni catalysts (12Ni-HT) were prepared by co-precipitation method, with the ratio of Ni : Mg : Al as 0.37 : 2.64 : 1. Details of catalyst preparation and characterization were described previously [51-53]. Different calcination temperatures were applied to control the Ni particle size, which were 773 K, 973 K, 1073 K and 1173 K, respectively. A summary of the Ni catalyst properties is listed in Table 1. Using Ni containing hydrotalcite like materials as the precursor, the obtained Ni particles are encapsulated in the oxide supports, making Ni particles highly stable [52]. The Ni particles with sizes between 8-12 nm are obtained. However, the method is difficult to obtain smaller Ni particles. The catalyst activity for steam methane reforming was measured in a fixed-bed reactor under atmospheric pressure. The detailed description of experimental set-up has been reported elsewhere [54]. 10 mg of Ni catalyst (0.05-0.15 mm) diluted with 100 mg of inert α-Al_2O_3 constituted the catalyst bed, which was reduced in 1/1 H_2/Ar (total flow: 200 cm^3/min) by increasing temperature from ambient to 943 K at 2 K/min and held under these conditions for 12h. The internal transport limitation was eliminated via preliminary kinetic study

performed on Ni catalysts using different pellet sizes. The external transport limitation was eliminated based on study with different flow rates and different space time. As a result, Ni catalysts with pellet size in the range of 50 to 150 μm and CH_4 flow larger than 100 cm^3/min were chosen for kinetic study. The reaction was carried out at 773 K, 798 K, 823 K, and 848 K, with S/C=3.5, and CH_4/H_2=1.0. The conversion is lower than 10% controlled by varying W/F_0. Concentrations of products were measured online by micro-gas chromatograph.

Table 1. Calcination temperature, Ni surface area, dispersion and particle size

Catalyst	Ni loading [wt% Ni/cat.]	Calcination temperature [K]	Ni surface area [$m^2/g_{cat.}$]	Ni surface area [m^2/g_{metal}]	Ni Dispersion [%]	d_{Ni}[a] [nm]
12Ni-HT_1	12	773	6.73	56.09	8.42	12
12Ni-HT_2	12	973	9.72	81.0	12.17	8.3
12Ni-HT_3	12	1073	7.14	59.54	8.94	11.3
12Ni-HT_4	12	1173	7.91	65.93	9.9	10.2

[a] Calculated from H_2 chemisorption, d_{Ni}(nm) = 101/D(%), where D is Ni dispersion.

2.2 Computational details

The preliminary microkinetic model of SMR was built on the basis of Rh(111), Ni(111), Pd(111), Pt(111), Cu(111), Fe (110), Co(0001) and Ru(0001) surfaces, including 26 elementary steps. All elementary steps can be found in Table S1 (Supporting information) as well as Fig. 5. In the model, direct CH_4 decomposition, OH*- and O*-assisted CH_4 decomposition were combined together to research CH_4 activation. Five possible routes, namely direct C-O combination pathway, CH-O pathway, C-OH pathway, and two CH-OH pathways were utilized to investigate CO formation. Moreover, the model simulated CO_2 formation from COOH* dissociation. To rapidly generate input parameters of the microkinetic model, a hybrid semi-empirical approach was employed in this work, using improved UBI-QEP method to calculate adsorption energies and BEP relationships to estimate activation energies [47].

Microkinetic modeling was performed on CatMAP, which output reaction rates by employing steady state to solve a mean-field model [48]. In the model, all electronic energies of gas-phase molecules and adsorbed species were corrected with zero point energies (E_{ZPE}), enthalpy (ΔH) and entropy (ΔS). Zero point energies were determined by vibrational frequencies, which were obtained from previous DFT computations towards adsorbed species [47]. The vibrational calculations were carried out on Pt (111) surface, and the same frequencies values were employed for other metal surfaces. Because the variations in zero point energies and entropic contributions among different metal surfaces were likely to be significantly smaller than that in adsorption energetics [55]. Experimental vibrational frequencies acquired from NIST database [56] were used for gas-phase species CH_4, H_2O, H_2, CO and CO_2. We applied Shomate equation to calculate gas-phase thermochemistry and harmonic approximation to describe thermochemistry of adsorbed species, assumed that all degrees of freedom were vibrational.

3. Results and Discussion

3.1 Experimental methods

Steam methane reforming was studied on four hydrotalcite-drived Ni catalysts, with Ni particle size as 8.3nm, 10.2nm, 11.3nm and 12nm, respectively. Towards each particle size, the catalyst activity was researched at four temperatures, namely 773 K, 798 K, 823 K, and 848 K. In the experiments, low conversion (< 10%) was employed to eliminate possible thermodynamic variations. CH_4 conversion rate was measured using the same method with that of Wang et al. [57]. As long as the net CH_4 conversion rate (r_n) was obtained, the forward CH_4 conversion rate (r_f) could be estimated by

$$r_f = \frac{r_n}{1-\eta} \tag{1}$$

Where η means the approach to equilibrium of SMR [10], which was controlled to be less than 0.1, and

described as following

$$\eta = \frac{P_{CO} P_{H_2}^3}{P_{CH_4} P_{H_2O}} \frac{1}{K_E} \quad (2)$$

Where P_{CO}, P_{H2}, P_{CH4} and P_{H2O} represent for partial pressure of CO, H_2, CH_4 and H_2O at the reactor outlet. K_E denotes thermodynamic equilibrium constant [58]. The forward methane turnover frequency (TOF_{CH4}^{Exp} ~~TOF_{CH4}~~) can be calculated from the forward CH_4 conversion rate (r_f), molecular weight of Ni (M_{Ni}), Ni weight fraction of the catalysts (f_{Ni}) and Ni dispersion (D), given by

$$TOF_{CH_4}^{Exp} = \frac{r_f M_{Ni}}{f_{Ni} D} \quad (3)$$

Fig. 1 (a) gives the forward methane turnover frequency (TOF_{CH4}^{Exp}) as a function of Ni particle size at different temperatures. The smaller the Ni particle size, the higher the TOF_{CH4}^{Exp} is observed in the experiments towards each temperature. This result is in agreement with that reported from Iglesia et al. [9] as well as Nørskov et al. [11]. Concerning each particle size, the Arrhenius plot is displayed as Fig. 1 (b). The measured experimental activation energies for SMR are 112.6 kJ/mol at 8.3 nm, 92 kJ/mol at 10.2 nm, 103.6 kJ/mol at 11.3 nm and 101.8 kJ/mol at 12 nm, respectively. These values are close to the data reported by Iglesis et al. (102 kJ/mol) [9], Linic et al. (101 ± 4 kJ/mol) [59] and Filippis et al. (96 ± 2 kJ/mol) [60].

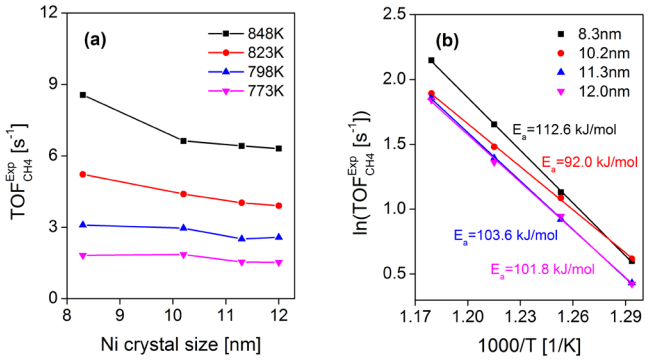

Fig. 1. Experimental (a) forward methane turnover frequency (TOF_{CH4}^{Exp}) as a function of Ni particle size at 773 K, 798 K, 823 K, and 848 K; (b) Arrhenius plot for four 12Ni-HT catalysts, with Ni particle size as 8.3 nm, 10.2 nm, 11.3 nm and 12 nm, respectively. Reaction condition: 1 bar, S/C=3.5, and CH_4/H_2=1.0.

Based on the Arrhenius plot, with particle size increasing, a decrease in activation energy is obtained, which should lead to an increase of TOF_{CH4}^{Exp}. Meanwhile, with increased particle size, a decrease in the pre-exponential factor is observed (Table S2 in supporting information), that will result in a decrease of TOF_{CH4}^{Exp}. Finally, the compensation effect [61, 62] between decreased activation energy and decreased pre-exponential factor leads to a decreased TOF_{CH4}^{Exp} along with increased particle size. The phenomenon demonstrates that pre-exponential, namely entropy change plays a more important role in catalyst activity than activation energy for SMR. The measured activation energy ~~Experimental data at~~ on Ni nanoparticle with a size of 10.2 nm is lower than expected ~~an exception~~, which might be due to a different ~~the change of~~ Ni nanoparticle shape or other reasons.~~during reaction or between different particle size, the experimental errors, or other reasons.~~ To further understand the size-dependent activity, Ni catalysts with different particle size are simulated and analyzed from theoretical points of view on the basis of microkinetic modeling.

3.2 Microkinetic modeling of steam methane reforming

The microkinetic model of steam methane reforming was built on the most close-packed surfaces of Ru, Rh, Ni, Pt, Pd, Co, Fe and Cu catalysts. The recommended C and O binding energies on these surfaces are employed to ensure the model accuracy. In the model, total energies of gas phase species were determined by DFT computations. Adsorption energies and activation energies were calculated by improved UBI-QEP method and BEP relationships, respectively. To keep data consistent, all energies were converted to 'generalized formation energies' with respect to gas phase H_2, H_2O and CH_4, and used as input parameters of microkientic model. The reaction temperature was 773 K, the total gas pressure was 1 bar and the gas composition was 63.6% H_2O, 18.2% CH_4 and 18.2% H_2. After simulation, the preliminary microkinetic

modeling results were obtained and subsequent model refinement was conducted by employing DFT calculated activation energy of RDS. The refined microkinetic model predicted reaction rate volcano is shown as Fig. 2 (a), which gives $Log(TOF_{CH_4}^{Cal})$ as a function of C- and O-metal formation energies. The relative activity among the 8 transition metal catalysts are: Ru ~ Rh > Ni ~ Pt > Pd ~ Co > Fe > Cu. The general activity tendency is consistent with experimental results reported by Nørskov et al. [11] and Lapszewicz et al. [4]. Thus, we could say that the model exhibits a reasonable degree of accuracy.

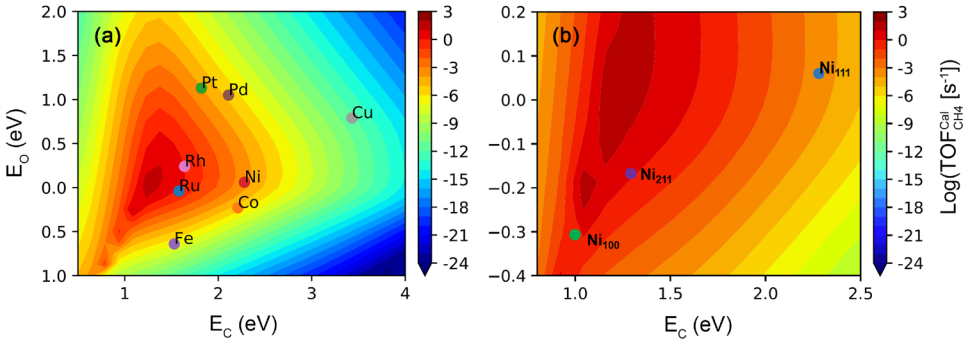

Fig. 2. Modeling predicted forward CH_4 conversion rate as a function of C and O formation energies in SMR on (a) Rh(111), Ni(111), Pd(111), Pt(111), Cu(111), Fe (110), Co(0001) and Ru(0001) surfaces; (b) Ni(111), Ni(211) and Ni(100) surfaces. Reaction condition: 773 K, 1 bar, S/C=3.5, and CH_4/H_2=1.0.

To simulate a real Ni particle, a truncated octahedron model involving Ni(111) and Ni(100) surfaces is selected in this study, where steps, edges and corners are treated as Ni(211) surface, same with the work of Green et al. [1]. At different particle size, the three surfaces fractions are different. Therefore, a model containing different surface fractions of Ni(111), Ni(100) and Ni(211) could be used to simulate Ni catalysts with different particle size. According to the reaction rate volcano displayed in Fig. 2 (a), $Log(TOF_{CH_4}^{Cal})$ is only associated with two descriptors. The activity of Ni(211) and Ni(100) could be easily predicted with C- and O-metal formation energies as descriptors. Using Fig. 2 (a) as a benchmark, the volcano plot is re-adjusted to focus on only the three Ni surfaces, as shown in Figure 2 (b). C and O formation energies on

Ni(211) are 1.32 eV and -0.18 eV, which are 1.00 eV and -0.31 eV for Ni(100) [47]. At 773 K, the modeling predicted activity is Ni(211) > Ni(100) > Ni(111). Afterwards, the microkinetic modeling was conducted at 798 K, 823 K and 848 K using the same methods. Ni(211) exhibits the highest activity than both Ni(111) and Ni(100) at all researched temperatures. The obtained TOF_{CH4}^{Cal} values are given in Table 2. As long as individual TOF_{CH4}^{Cal} are acquired over the three surfaces, the total TOF_{CH4}^{Cal} can be calculated and analyzed at different Ni particle size, which will give insight into size-dependent activity.

3.3 Modeling driven size-dependent activity

The interaction between intermediates over adjacent surfaces can be processed as either (1) no interaction (no diffusion) [18], (2) a fast surface diffusion, assuming same intermediates coverage on all surfaces [29], (3) treating diffusion as a reaction from one surface to another [1]. To simplify calculation, we directly use the 'no diffusion' model, considering that reactions occur on the three surfaces separately. With individual reaction rates obtained over the three surfaces, the total reaction rate (TOF_{CH4}^{Cal}) can be estimated by the sum of surface fraction (f_i) times individual reaction rate (TOF_i), similar to the work of Ligthart et al. [18]:

$$TOF_{CH_4}^{Cal} = \sum_{i=1}^{3} f_i * TOF_i = f_{111} * TOF_{111} + f_{100} * TOF_{100} + f_{211} * TOF_{211} \quad (4)$$

Where f_{111}, f_{100} and f_{211} are surface fractions of (111), (100) and (211), respectively, estimated by a truncated octahedron model. TOF_{111}, TOF_{100} and TOF_{211} are individual turnover frequencies on (111), (100) and (211) surfaces, predicted by microkinetic modeling. Table S4 gives the three surfaces fractions with respect to particle size. After calculation, total TOF_{CH4}^{Cal} ~~TOF_{total}^{Cal}~~ for steam methane reforming at different Ni particle sizes and temperatures are gained and displayed in Table 2 as well as Fig. 3 (a). The results illustrate that the smaller the Ni particles, the higher the activity. With temperature increasing, activity difference between small particles and large particles is enlarged. This is in good agreement with previous experimental results. If we compare the absolute TOF_{CH4} values between experiments and microkinetic modeling, even

though there are some difference between them, their ratios (TOF_{CH4}^{Exp}~~TOF_{exp}~~/TOF_{CH4}^{Cal}) are almost 16 ± 2. That is to say, the model can correctly predict the activity trend relative to particle size. A number of sources of error that existed in both experiments and modeling might cause the absolute TOF_{CH4} values difference. Fig. 3 (b) gives the Arrhenius plot at each particle size. The calculated activation energies are 117.4 kJ/mol at 8.4 nm, 114.3 kJ/mol at 9.8 nm, 111.4 kJ/mol at 11.1 nm and 108.8 kJ/mol at 12.4 nm, respectively. The microkinetic model predicted well the tendency of the change in the apparent activation energy with Ni particle size, namely higher activation energy on smaller sized Ni particles. However, ~~The~~the model predicted activation energies are slightly higher than the ~~differences between~~ experimental values. ~~and modeling results are within 10 kJ/mol, except for that at 10.2/9.8 nm (~ 20 kJ/mol)~~. In the modeling, the Ni nanoparticle shape is assumed same towards different particle sizes, simulated by a truncated octahedron model. The change of particle shape during the reaction has been ignored. ~~is neglected.~~ However, in the real reaction, the catalyst might modify its morphology [63], possibly leading to the change of activity as well as effective activation energy. In addition, possible contributions of the support to the reaction, such as water activation was not considered in the model. These simplifications could result in the deviation of predicted activation energy from the experimental values. ~~Therefore, the differences between experimental and calculated activation energies are observed. Due to the observed small differences, the modeling results are considered acceptable. It can be concluded that the modeling exhibits a reasonable accuracy for predicting the particle size effect on activity as well as effective activation energies, which fit experiments well.~~

Table 2. Modeling predicted forward methane turnover frequency (TOF_{CH4}^{Cal}) for steam methane reforming on

different Ni surfaces and particle size at 773 K, 798 K, 823 K and 848 K

Ni/TOF_{CH4}^{Cal} [s^{-1}]	Ni Surface			Particle size (nm)			
	Ni(111)	Ni(100)	Ni(211)	8.4	9.8	11.1	12.4
773 K	0.025	0.194	0.706	0.111	0.104	0.099	0.095
798 K	0.045	0.135	1.398	0.180	0.165	0.153	0.144
823 K	0.079	0.094	2.669	0.315	0.284	0.261	0.242
848 K	0.134	0.067	4.931	0.557	0.500	0.456	0.421

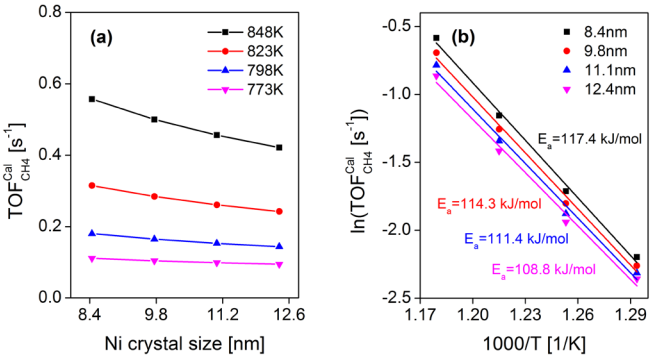

Fig. 3. Modeling predicted (a) forward methane turnover frequency (TOF_{CH4}^{Cal}) as a function of Ni particle size at 773 K, 798 K, 823 K, and 848 K; (b) Arrhenius plot for four Ni catalysts, with Ni particle size as 8.4 nm, 9.8 nm, 11.1 nm and 12.4 nm, respectively. Reaction condition: 1 bar, S/C=3.5, and CH_4/H_2=1.0.

The particle size effect on activity can be analyzed from individual surface contribution to activity. Fig. 4 (a), (b) and (c) give Ni(111), Ni(100) and Ni(211) surface contributions to total TOF_{CH4}^{Cal} against Ni crystal size. When the Ni crystal size is 8.4 nm, Ni(211) provides the major activity of Ni catalysts towards all researched temperatures. As Ni crystal size increasing, the contribution of Ni(211) is gradually reduced due to decreased Ni(211) surface fraction. In contrast, the contributions of Ni(111) and Ni(100) are enhanced because of increased Ni(111) and Ni(100) surface fractions. When the Ni crystal size is increased to 12.4 nm, both Ni(211) and Ni(100) play important roles to support Ni activity at 773 K. However, at 798 K, 823 K and 848 K, Ni(211) still contributes most to Ni activity. The results indicate that Ni(211) is the most active

surface occurred in SMR reaction, same with the conclusion of Nørskov et al. [11]. The much lower activity of Ni(111) and Ni(100) relative to Ni(211) leads to the dropped activity of larger particles.

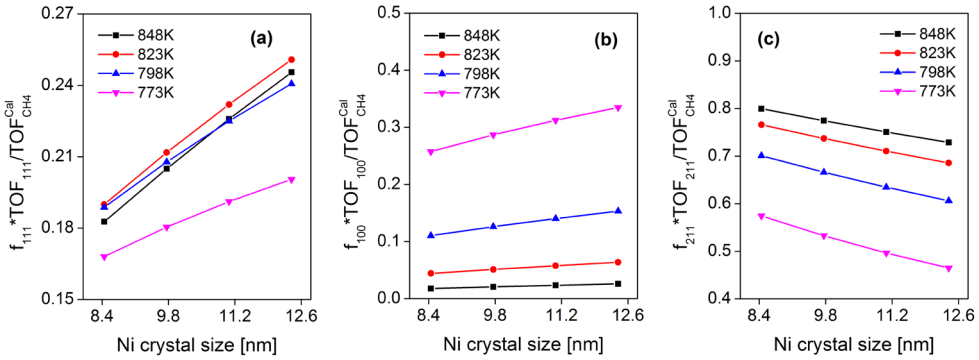

Fig. 4. Surface contribution on total TOF_{CH4}^{Cal} as a function of Ni crystal size for (a) Ni(111), (b) Ni(100) and (c) Ni(211) at 773 K, 798 K, 823 K and 848 K. Reaction condition: 1 bar, S/C=3.5, and CH_4/H_2=1.0.

3.4 Size-dependent mechanism research

Size-dependent activity is related to the changed surface fractions with respect to particle size as well as individual reaction rates over the three Ni surfaces. Much higher activity of Ni(211) than Ni(111) and Ni(100) accompanied by decreased Ni(211) surface fraction results in reduced Ni activity as Ni particle size increasing. To explain the activity trend among different Ni surfaces, a better understanding of steam methane reforming mechanism is necessary to aid. Figure 5 displays the SMR reaction network used in microkinetic model. The modeling predicted net turnover frequency (TOF_{Net}^{Cal}) of each elementary step over Ni(211) surface at 773 K is listed as well. Through comparing the reaction rates of different routes, the dominant reaction pathway can be obtained. Towards CH_4 activation, direct CH_4 decomposition is observed much more favorable than O*- and OH*-assisted CH_4 decomposition. Concerning CO formation, the CH-O pathway, namely CH* + O* ↔ HCO* + * ↔ CO* + H* exhibits much higher TOF_{Net}^{Cal} than other pathways. CO_2 formation rate is much lower than that of CO, demonstrating a low activity of water gas shift reaction,

which is almost negligible. Consequently, the dominant reaction pathway of steam methane reforming is predicted as $CH_4(g) \rightarrow CH_3^* \rightarrow CH_2^* \rightarrow CH^* \rightarrow HCO^* \rightarrow CO^*$ over Ni(211) surfaces based on microkinetic modeling, which is colored blue in Fig. 5. The same conclusions are achieved over Ni(111) and Ni(100) surfaces, according to the reaction rates given in Table S1 (Supporting information). As the temperature rises to 798 K, 823 K and 848 K, the dominant pathway remains the same.

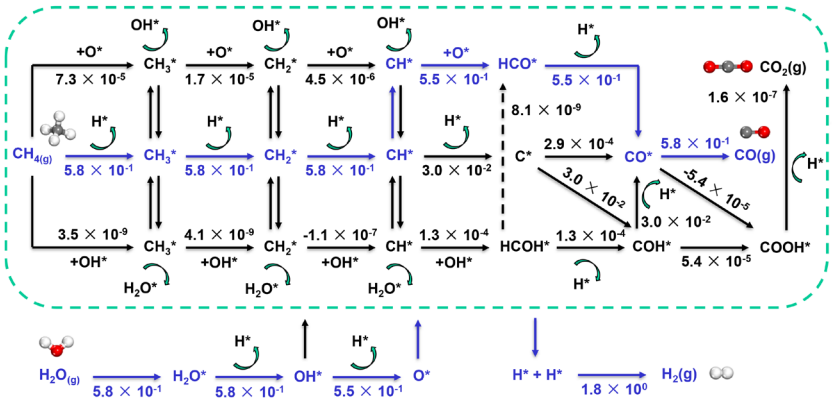

Fig. 5. Reaction network for steam methane reforming over Ni catalyst, as well as estimated net turnover frequency (TOF_{Net}^{Cal}) for elementary steps involved in the microkinetic model over Ni(211) surface at 773 K. The dominant reaction pathway is colored blue. Reaction condition: 773 K, 1 bar, S/C=3.5, and CH_4/H_2=1.0.

Free energy diagrams are plotted to intuitively reveal the mechanism of CH_4 activation and CO formation. Ni(211), as the most active Ni surface, is employed as an example to give the free energy plots at 773 K. Fig. 6 (a) displays the free energy diagram of three CH_4 decomposition routes combined with CH-O route on Ni (211) surface. The blue, red and black routes correspond to direct CH_4 decomposition, O*-assisted and OH*-assisted CH_4 decomposition, respectively. From the free energy diagram, how to find the rate-determining step (RDS) and relate the free energy with total reaction rate is a key issue.

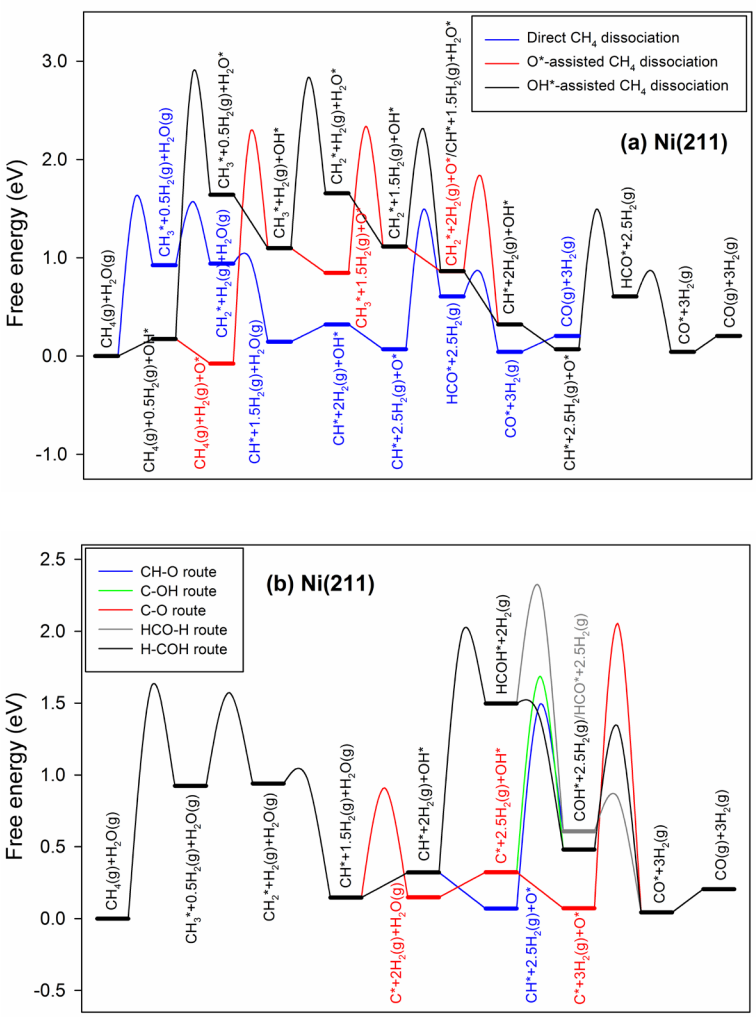

Fig. 6. Free energy diagrams of SMR on Ni(211) surface towards (a) three CH_4 activation routes + CH-O route. The blue, red and black routes correspond to direct CH_4 decomposition, O*-assisted and OH*-assisted CH_4 decomposition, respectively; (b) direct CH_4 decomposition + five CO formation routes. The blue, green, red, gray and black ones represent for CH-O route, C-OH route, C-O route, HCO-H route and H-COH route respectively. Reaction condition: 773 K, 1 bar, S/C=3.5, and CH_4/H_2=1.0.

For direct CH_4 decomposition, if we treat ES6 ($CH^* + 2.5H_2(g) + O^* \rightleftarrows HCO^* + 2.5H_2(g) + *$) as rate

determining step, and other steps as quasi-equilibrated. Then the reaction (I) involving elementary steps before ES6, namely $CH_4(g) + H_2O(g) + 2* \rightleftarrows CH* + 2.5H_2(g) + O*$ could be assumed equilibrium, with the equilibrium constant written as:

$$K_{\mathrm{I}} = \frac{P_{H_2}^{2.5}\theta_{CH}\theta_O}{P_{CH_4}P_{H_2O}\theta_*^2} = \exp\left(\frac{-\Delta G_{\mathrm{I}}}{k_B T}\right) \tag{5}$$

Where θ is the surface coverage, P is pressure, T is temperature, and k_B is Boltzmann constant. ΔG_{I} represents for the free energy change of reaction I.

The forward reaction rate of ES6 is:

$$r_6^+ = k_6^+ P_{H_2}^{2.5}\theta_{CH}\theta_O \tag{6}$$

$$k_6^+ = \frac{k_B T}{h}\exp\left(\frac{-\Delta G_6^{Act}}{k_B T}\right) \tag{7}$$

Where h denotes Planck's constant. ΔG_6^{Act} means the free energy of activation for ES6.

With combination of equation (5) and (7), equation (6) could be expressed as:

$$r_6^+ = \frac{k_B T}{h}\exp\left(\frac{-\Delta G_6^{Act} - \Delta G_{\mathrm{I}}}{k_B T}\right) P_{CH_4}P_{H_2O}\theta_*^2 \tag{8}$$

$$\Delta G_6^{Act} + \Delta G_{\mathrm{I}} = G_{TS} - G_{CH_4} - G_{H_2O} \tag{9}$$

Where G_{TS}, G_{CH4} and G_{H2O} stand for the free energy of ES6 transition state, gas-phase CH_4 and H_2O, respectively. As shown in Fig. 6 (a) and (b), free energy of gas-phase CH_4 and H_2O are assumed to be 0. Therefore, r_6^+ is only related to G_{TS}, P_{CH4}, P_{H2O} and $\theta*$. For reaction occurs on a specific metal surface, the gas pressure (P_{CH4}, P_{H2O}) and vacancy coverage ($\theta*$) are same towards different elementary steps. In consequence, the higher the transition state free energy, the lower the reaction rate. The elementary step with

highest transition state free energy (G_{HTS}) is the rate-determining step (RDS).

Direct CH_4 decomposition is energetically more preferred than O*-assisted and OH*-assisted CH_4 decomposition because of its lower free energy level (RDS), as shown in Fig. 6 (a). This result is consistent with that reported by Vlachos et al. on Pt(111) and Pt(211) surface [64], and by Neurock et al. over Ru, Rh, Pd, Os, Ir, and Pt terrace surfaces [65]. As direct CH_4 decomposition proceeds, the resulting C* or CH* can subsequently undergo five possible routes to form CO. Fig. 6 (b) gives the free energy diagram of five CO formation routes combined with direct CH_4 decomposition on Ni(211) surface. HCO-H route (gray), H-COH (black) and C-O route (red) are energetically much less favorable than CH-O route (blue) and C-OH route (green), which results in their extremely low reaction rates. The phenomenon is in agreement with that reported by Green et al. over Ni(211) surface at 773 K [1]. CH-O route is the energetically most preferred one due to the lowest free energy level, consistent with the study of Vlachos et al. on Pt(211) surface [64]. The similar free energy analysis is then performed on Ni(111) and Ni(100) surfaces as well as 798 K, 823 K and 848 K, which indicates that direct CH_4 decomposition + CH-O route is the major reaction pathway for them all. The free energy diagrams interpret previous modeling results. It also demonstrates that SMR reaction mechanism is size independent for Ni catalysts from 773 K to 848 K. No matter at small or large particle size, SMR reaction mainly takes place via $CH_4(g) \rightarrow CH_3^* \rightarrow CH_2^* \rightarrow CH^* \rightarrow HCO^* \rightarrow CO^*$ on Ni catalysts, owing to its lowest free energy level.

3.5 Size-dependent activity analysis

Size-dependent activity is mainly resulted from surface-dependent activity, as described previously. To analyze the surface-dependent activity, free energy diagrams of dominant reaction pathway of SMR are plotted on three Ni surfaces at 773 K (solid line) and 848 K (dashed line), shown as Fig. 7. At 773 K, HCO* formation ($CH^* + O^* \rightarrow HCO^*$) is RDS on Ni(111) surface, and CH_4 dissociation ($CH_4(g) \rightarrow CH_3^* + H^*$) is RDS on Ni(211) and Ni(100) surfaces. With temperature increasing, the RDS on Ni(111) surface is

changed to CH_3 dissociation ($CH_3^* \rightarrow CH_2^* + H^*$), while that on Ni(211) and Ni(100) surfaces remains the same. According to previous analysis, at smaller particle size (8.4 nm), Ni(211) is the most active surface; at larger particle size (12.4 nm), both Ni(211) and Ni(100) control Ni activity (773 K). CH_4 dissociation is therefore considered as RDS for Ni catalysts, which is size-independent. This finding is in good agreement with the study of Iglesia et al. [10].

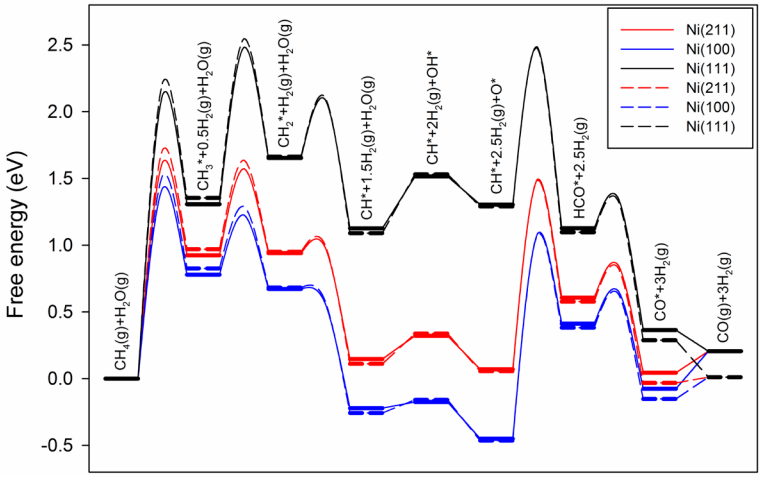

Fig. 7. Free energy diagrams of direct CH_4 decomposition + CH-O route in steam methane reforming over three Ni surfaces at 773 K (solid line) and 848 K (dashed line). Ni(111), Ni(100) and Ni(211) are colored black, blue, and red, respectively. Reaction condition: 1 bar, S/C=3.5, and CH_4/H_2=1.0.

The free energy plots exhibit G_{HTS} as Ni(111) > Ni(211) > Ni(100) at both 773 K and 848 K. If we treat activity inversely proportional to G_{HTS}, the activity is predicted as Ni(100) > Ni(211) > Ni(111). However, the microkinetic modeling obtained activity trend is Ni(211) > Ni(100) > Ni(111) at 773 K and Ni(211) > Ni(111) > Ni(100) at 848 K. This is because activity is not only related to free energy (G_{HTS}), but also to vacancy coverage (θ^*). Table 3 gives the values of free energy (G_{HTS}), microkinetic modeling predicted main surface species coverage and vacancy coverage, as well as TOF_{CH4}^{Cal} at 773 K and 848 K. It can be seen that

the lower activity of Ni(100) than Ni(211) is caused by lower vacancy coverage on Ni(100) compared to that of Ni(211). The extremely low vacancy coverage on Ni(100) is resulted from its strong C binding ability, with surface mainly covered by C* and CH* species. The carbon deposition phenomenon appeared on Ni(100) has been reported by Schouten et al. towards methane decomposition [66, 67]. Moreover, Eizenberg and Blakely observed monolayer graphite formation on Ni(100) surface in experiments [68, 69]. Ni(111) is energetically much less favored than Ni(211), showing lower activity. To sum up, The activity of Ni(111) is limited by high free energy barrier (G_{HTS}). The activity of Ni(100) is controlled by surface site blocking. Ni(211) exhibits the highest activity owing to both moderate free energy barrier and vacancy coverage.

Table 3. The values of RDS transition state free energy (G_{HTS}), microkinetic modeling predicted main surface species coverage and vacancy coverage (θ_*), as well as forward CH_4 conversion rate ($TOF_{CH_4}^{Cal}$) over Ni(111), Ni(100) and Ni(211) surfaces at 773 K and 848 K

Ni surfaces	773 K			848 K		
	Ni(111)	Ni(100)	Ni(211)	Ni(111)	Ni(100)	Ni(211)
G_{HTS}/eV	2.49	1.43	1.62	2.55	1.52	1.71
θ_{C*}	1.47E-08	0.636	1.78E-04	7.81E-08	0.789	4.04E-04
θ_{CH*}	4.06E-09	0.333	7.84E-05	1.12E-08	0.202	8.84E-05
θ_{O*}	0.189	1.79E-04	0.842	0.181	8.98E-06	0.793
θ_{H*}	0.031	0.020	0.055	0.021	0.004	0.046
θ_*	0.777	0.012	0.095	0.795	0.005	0.153
$TOF_{CH_4}^{Cal}$/s^{-1}	0.025	0.194	0.706	0.134	0.067	4.931

As temperature increases from 773 K to 848 K, G_{HTS} values increase. Meanwhile, vacancy coverage on Ni(100) surface decreases. Combination of G_{HTS} and θ_* leads to reduced activity of Ni(100). In contrast, vacancy coverages over Ni(111) and Ni(211) surfaces increase, which result in enhanced activity by combination of increased G_{HTS}. Therefore, with temperature rising, Ni(111) and Ni(211) provide more contribution to Ni activity, and the total activity of Ni is increased due to much enhanced Ni(211) activity.

Ni(211) is the most active surface appeared in Ni catalysts, which is confirmed by previous analysis. Decreased Ni(211) surface fraction leads to dropped Ni activity as particle size increasing, which explains the size-dependent activity. In order to find a suitable size, a larger range of Ni particle size (1.3-16 nm) is employed to investigate the size-dependent activity based on modeling, shown as Fig. 8. The smaller the particle size, the higher the activity, and the larger the activity difference between adjacent points is observed, where the size differences between adjacent points are similar. The figure indicates that Ni particles with size smaller than 6 nm display fast-growing activity as size decreasing. While Ni particles with size larger than 12 nm tend to have almost stable activity. As a result, stabilizing small Ni particles (≤ 6 nm) could be a good strategy to obtain highly active Ni catalysts for steam methane reforming reactions.

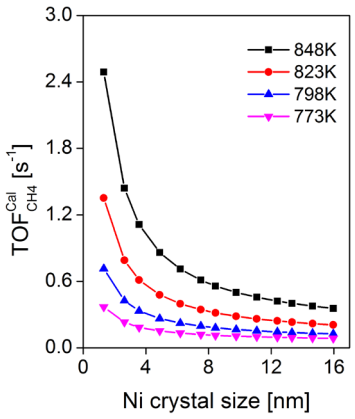

Fig. 8. Modeling predicted forward methane turnover frequency (TOF_{CH4}^{Cal}) as a function of Ni particle size (1.3-16 nm) at 773 K, 798 K, 823 K, and 848 K. Reaction condition: 1 bar, S/C=3.5, and CH_4/H_2=1.0.

Based on the above experimental and microkinetic modeling analysis, the size dependent activity depends on the relatively rate of the various facets of Ni particles, such as Ni (211), (100) and (111) as well as the number of active sites on these facets. The method developed here can be expected to rationalize the effect of support on the particle shapes and possible change in shape of particles during reactions. It has been recently reported by Maestri and coworkers [63] that the morphology of Rh/α-Al_2O_3 changed with reaction

conditions in catalytic partial oxidation of methane by using combined Wulff–Kaishew construction, ab initio thermodynamics and microkinetic modeling. The change in particle shape resulted mainly in the change in fraction of different facets, thus the changes in the activity. This could also explain the variation in the reported apparent activation energy and TOF sequences in the literature [9,59,60], possibly due to differences in the partial size and the shape.

Formatted: Highlight

4. Conclusions

The size-dependent activity of steam methane reforming is firstly investigated on hydrotalcite-drived Ni catalysts, with Ni particles prepared from 8.3 nm to 12 nm. The smaller the Ni particle size, the higher the activity is observed. The measured experimental activation energies are 112.6 kJ/mol at 8.3 nm, 92 kJ/mol at 10.2 nm, 103.6 kJ/mol at 11.3 nm and 101.8 kJ/mol at 12 nm, respectively. Afterwards, a truncated octahedron model is applied to simulate the similar size Ni particles, using microkinetic modeling to predict their activity. Input parameters of the microkinetic model are estimated from a combined UBI-QEP + BEP approach. Based on the model, smaller Ni particles display better performance than larger particles. It demonstrates that the modeling exhibits a reasonable accuracy for prediction of particle size effect on activity as well as effective activation energies, which fit experiments very well.

Theoretical investigation illustrates that the size-dependent activity is related to surface-dependent activity as well as changed surface fractions with respect to particle size. Ni(211) is the most active surface, which provides the major activity of Ni catalysts at small particle size. Towards larger particles, both Ni(211) and Ni(100) play important roles to contribute to Ni activity. Much higher activity of Ni(211) than Ni(111) and Ni(100) accompanied by decreased Ni(211) surface fraction results in reduced Ni activity as Ni particle size increasing. In addition, SMR mechanism is found to be independent of Ni particle size, which mainly occurs via $CH_4(g) \rightarrow CH_3^* \rightarrow CH_2^* \rightarrow CH^* \rightarrow HCO^* \rightarrow CO^*$, with CH_4 dissociation as rate determining step. Based on the screened mechanism, Ni(211) exhibits the highest activity due to its moderate free energy

barrier and surface vacancy coverage. In contrast, the activity of Ni(111) is limited by high free energy barrier, while that of Ni(100) is limited by surface blockage of C* and CH* species. In view of the fact that smaller Ni particles exhibit higher activity, finding proper approaches to prepare extremely small Ni particles (⩽ 6 nm) might be a good strategy to improve steam methane reforming efficiency.

Acknowledgements. The supports from NTNU energy, Norwegian research council, and the Natural Science Foundation of China (91645122 and U1663221), as well as the computational time provided by the Notur project are highly acknowledged.

References

[1] D. W. Blaylock, Y. A. Zhu, W. H. Green, Top. Catal. 54 (2011) 828.

[2] J. R. Rostrup-Nielsen, J. Catal. 31 (1973) 173-199.

[3] J. R. Rostrupnielsen, J. H. B. Hansen, J. Catal. 144 (1993) 38-49.

[4] D. Qin, J. Lapszewicz, Catal. Today 21 (1994) 551-560.

[5] J. Wei, E. Iglesia, J. Phys. Chem. B 108 (2004) 7253-7262.

[6] J. Wei, E. Iglesia, J. Catal. 225 (2004) 116-127.

[7] J. Wei, E. Iglesia, J. Phys. Chem. B 108 (2004) 4094-4103.

[8] J. Wei, E. Iglesia, Phys. Chem. Chem. Phys. 6 (2004) 3754-3759.

[9] J. Wei, E. Iglesia, Angew. Chem. Int. Ed. 43 (2004) 3685-3688.

[10] J. Wei, E. Iglesia, J. Catal. 224 (2004) 370-383.

[11] G. Jones, J. G. Jakobsen, S. S. Shim, J. Kleis, M. P. Andersson, J. Rossmeisl, F. Abild-Pedersen, T. Bligaard, S. Helveg, B. Hinnemann, J. R. Rostrup-Nielsen, I. Chorkendorff, J. Sehested, J. K. Nørskov, J. Catal. 259 (2008) 147-160.

[12] C. A. Wolcott, A. J. Medford, F. Studt, C. T. Campbell, J. Catal. 330 (2015) 197-207.

[13] Y. Xu, A. C. Lausche, S. Wang, T. S. Khan, F. Abild-Pedersen, F. Studt, J. K. Nørskov, T. Bligaard, New J. Phys. 15 (2013) 125021.

[14] J. K. Nørskov, C. H. Christensen, Science 312 (2006) 1322-1323.

[15] J. Sehested, Catal. Today 111 (2006) 103-110.

[16] K. O. Christensen, D. Chen, R. Lødeng, A. Holmen, Appl. Catal. A: Gen. 314 (2006) 9-22.

[17] D. Baudouin, U. Rodemerck, F. Krumeich, A. de Mallmann, K. C. Szeto, H. Ménard, L. Veyre, J. P. Candy, P. B.Webb, C. Thieuleux, C. Copéret, J. Catal. 297 (2013) 27-34.

[18] D. A. J. M. Ligthart, R. A. Van Santen, E. J. M. Hensen, J. Catal. 280 (2011) 206-220.

[19] H. S. Bengaard, J. K. Nørskov, J. Sehested, B. S. Clausen, L. P. Nielsen, A. M. Molenbroek, J. R. Rostrup-Nielsen, J. Catal. 209 (2002) 365-384.

[20] D. Chen, K. O. Christensen, E. Ochoa-Fernández, Z. Yu, B. Tøtdal, N. Latorre, A. Monzón, A. Holmen, J. Catal. 229 (2005) 82-96.

[21] C. J. Liu, J. Ye, J. Jiang, Y. Pan, ChemCatChem 3 (2011) 529-541.

[22] O. Choi, Z. Hu, Environ. Sci. Technol. 42 (2008) 4583-4588.

[23] P. Lara, K. Philippot, B. Chaudret, ChemCatChem 5 (2013) 28-45.

[24] C. J. H. Jacobsen, S. Dahl, P. L. Hansen, E. Törnqvist, L. Jensen, H. Topsøe, D. V. Prip, P. B. Møenshaug, I. Chorkendorff, J. Mol. Catal. A: Chem. 163 (2000) 19-26.

[25] K. Honkala, A. Hellman, I. N. Remediakis, A. Logadottir, A. Carlsson, S. Dahl, C. H. Christensen, J. K. Nørskov, Science 307 (2005) 555-558.

[26] J. Greeley, J. Rossmeisl, A. Hellmann, J. K. Norskov, Z. Phys. Chem. 221 (2007) 1209-1220.

[27] D. W. Blaylock, T. Ogura, W. H. Green, G. J. O. Beran, J. Phys. Chem. C 113 (2009) 4898-4908.

[28] D. Chen, R. Lødeng, H. Svendsen, A. Holmen, Ind. Eng. Chem. Res. 50 (2010) 2600-2612.

[29] C. Fan, Y. A. Zhu, M. L. Yang, Z. J. Sui, X. G. Zhou, D. Chen, Ind. Eng. Chem. Res. 54 (2015) 5901-5913.

[30] A. A. Gokhale, J. A. Dumesic, M. Mavrikakis, J. Am. Chem. Soc. 130 (2008) 1402-1414.

[31] J. K. Nørskov, T. Bligaard, J. Rossmeisl, C. H. Christensen, Nature Chem. 1 (2009) 37-46.

[32] J. K. Nørskov, F. Abild-Pedersen, F. Studt, T. Bligaard, Proc. Nat. Acad. Sci. (2011) 201006652.

[33] E. Shustorovich, Surf. Sci. Rep. 6 (1986) 1-63.

[34] E. Shustorovich, Adv. Catal. 37 (1990) 101-163.

[35] E. M. Shustorovich, A. V. Zeigarnik, Russ. J. Phys. Chem. 80 (2006) 4-30.

[36] F. Abild-Pedersen, J. Greeley, F. Studt, J. Rossmeisl, T. R. Munter, P. G. Moses, E. Skúlason, T. Bligaard, J. K. Nørskov, Phys. Rev. Lett. 99 (2007) 016105.

[37] E. M. Fernández, P. G. Moses, A. Toftelund, H. A. Hansen, J. I. Martínez, F. Abild-Pedersen, J. Kleis, B. Hinnemann, J.

Rossmeisl, T. Bligaard, J. K. Nørskov, Angew. Chem., 120 (2008) 4761-4764.
[38] G. Jones, T. Bligaard, F. Abild-Pedersen, J. K. Nørskov, J. Phys. Condens. Matter 20 (2008) 064239.
[39] C. Muller, V. Michel, G. Scacchi, G. M. Côme, J. Chim. Phys. 92 (1995) 1154-1178.
[40] J. Kua, F. Faglioni, W. A. Goddard, J. Am. Chem. Soc. 122 (2000) 2309-2321.
[41] M. Salciccioli, Y. Chen, D. G. Vlachos, J. Phys. Chem. C 114 (2010) 20155-20166.
[42] V. Pallassana, M. Neurock, J. Catal. 191 (2000) 301-317.
[43] A. Michaelides, Z. P. Liu, C. J. Zhang, A. Alavi, D. A. King, P. Hu, J. Am. Chem. Soc. 125 (2003) 3704-3705.
[44] K. Lee, E. Lee, C. Song, M. J. Janik, J. Catal. 309 (2014) 248-259.
[45] Z. W. Ulissi, A. J. Medford, T. Bligaard, J. K. Nørskov, Nat. Commun. 8 (2017) 14621.
[46] M. Maestri, K. Reuter, Angew. Chem. Int. Ed. 50 (2011) 1194-1197.
[47] Y. Wang, L. Xiao, Y. Qi, M. Mahmoodinia, X. Feng, J. Yang, Y. Zhu, D. Chen, (Submitted).
[48] A. J. Medford, C. Shi, M. J. Hoffmann, A. C. Lausche, S. R. Fitzgibbon, T. Bligaard, J. K. Nørskov, Catal. Lett. 145 (2015) 794-807.
[49] A. R. Singh, J. H. Montoya, B. A. Rohr, C. Tsai, A. Vojvodic, J. K. Nørskov, ACS Catal. 8 (2018) 4017-4024.
[50] L. Yu, F. Abild-Pedersen, ACS Catal. 7 (2017) 864-871.
[51] E. Ochoa-Fernández, C. Lacalle-Vilà, K. O. Christensen, J. C. Walmsley, M. Rønning, A. Holmen, D. Chen, Top. Catal. 45 (2007) 3-8.
[52] R. Dehghan-Niri, J. C. Walmsley, A. Holmen, P. A. Midgley, E. Rytter, A. H. Dam, A. B. Hungria, J. C. Hernandez-Garrido, D. Chen, Catal. Sci. Technol. 2 (2012) 2476-2484.
[53] J. Niu, S. E. Liland, J. Yang, K. R. Rout, J. Ran, D. Chen, Chem. Eng. J. (2018) In press.
[54] J. R. Rostrup-Nielsen, J. Sehested, J. K. Nørskov, Adv. Catal. 47 (2002) 65-139.
[55] T. Bligaard, K. Honkala, A. Logadottir, J. K. Nørskov, S. Dahl, C. J. H. Jacobsen, J. Phys. Chem. B 107 (2003) 9325-9331.
[56] P. J. Linstrom, W. G. Mallard. NIST Chemistry webbook; NIST standard reference database No. 69, 2001. https://doi.org/10.18434/T4D303.
[57] H. Wang, D. W. Blaylock, A. H. Dam, S. E. Liland, K. R. Rout, Y. A. Zhu, W. H. Green, A. Holmen, D. Chen, Catal. Sci. Technol. 7 (2017) 1713-1725.
[58] L. M. Aparicio, J. Catal. 165 (1997) 262-274.
[59] E. Nikolla, J. Schwank, S. Linic, J. Catal. 263 (2009) 220-227.
[60] M. Zeppieri, P. L. Villa, N. Verdone, M. Scarsella, P. De Filippis, Appl. Catal. A: Gen. 387 (2010) 147-154.
[61] B. R. Cuenya, F. Behafarid, Surf. Sci. Rep. 70 (2015) 135-187.
[62] P. J. Schmitz, R. J. Kudla, A. R. Drews, A. E. Chen, C. K. Lowe-Ma, R. W. McCabe, W. F. Schneider, C. T. Goralski Jr, Appl. Catal. B: Envion. 67 (2006) 246-256.
[63] R. Cheula, A. Soon, M. Maestri, Catal. Sci. Technol. 8 (2018) 3493-3503.
[64] Y. Chen, D. G. Vlachos, Ind. Eng. Chem. Res. 51 (2012) 12244-12252.
[65] D. Hibbitts, M. Neurock, Surf. Sci. 650 (2016) 210-220.
[66] F. C. Schouten, O. L. J. Gijzeman, G. A. Bootsma, Bull. Soc. Chim. Belg. 88 (1979) 541-547.
[67] F. C. Schouten, O. L. J. Gijzeman, G. A. Bootsma, Surf. Sci. 87 (1979) 1-12.
[68] M. Eizenberg, J. M. Blakely, J. Chem. Phys. 71 (1979) 3467-3477.
[69] I. Alstrup, J. Catal. 109 (1988) 241-251.

Supporting Information

Understanding Effects of Ni Particle Size on Steam Methane Reforming Activity by Combined Experimental and Theoretical Analysis

Yalan Wang[1], Hongmin Wang[1], Anh Hoang Dam[1], Ling Xiao[2], Yanying Qi[1], Juntian Niu[1], Jia Yang[1], Yi-An Zhu[2,*], Anders Holmen[1], De Chen[1,*]

[1] *Department of Chemical Engineering, Norwegian University of Science and Technology (NTNU), N-7491 Trondheim, Norway*

[2] *State Key Laboratory of Chemical Engineering, East China University of Science and Technology, Shanghai, 200237, China*

To whom correspondence should be addressed: yanzhu@ecust.edu.cn and de.chen@ntnu.no

1. Estimation of adsorption energies

UBI-QEP method is developed based on three assumptions. Firstly, in a many-body system, forces depend only on distance; Secondly, each M-A two-center interaction is described by a Morse potential, and the total adsorption heat of many-body system is estimated by the sum of all M-A two-center interactions. Thirdly, during the interaction of an adsorbed species with a metal surface, the total bond index, x, is conserved at unity. According to the three assumptions, Shustorovich and Sellers [1-3] proposed standard UBI-QEP equations, where atomic binding energies (Q_A) of C-, H-, and O-metal are descriptors to estimate binding energies of C-, H-, and O-containing species. On the basis of standard UBI-QEP equations, an improved UBI-QEP method was proposed in our prior work to estimate adsorption energies, by using DFT data as a systematic benchmark [4]. In that work, the atomic binding energies (Q_A) were estimated by DFT calculations. To further increase the model accuracy, optimized Q_A values are suggested here. For Cu, the recommended Q_A value by Shustorovich [5-7] is directly applied; For Ru and Fe, Q_A are empirical values, which are modified according to the fitting data. For Co, Ni, Rh, Pd and Pt, DFT calculated Q_A values are still used. The optimized Q_A values are recommended in this work for estimation of adsorption heats.

2. Fast prediction of activation energies

As long as adsorption energies are achieved via the improved UBI-QEP method, reaction heats could be easily estimated and further used for fast prediction of activation energies by means of BEP relationships. In our prior study [4], general BEP relationships towards C-H, C-O, C-C bond cleavage and O-H bond recombination were obtained. However, except for above 4 type reactions, C-O-H bond activation is another typical reaction existed in SMR, such as elementary steps 8-13 (Table S1). Towards these reactions, the unified BEP relation is provided in Fig. S1, namely $E_a = 0.66\Delta H + 1.38$. All BEP relationships are then applied to calculate activation energies, with combination of UBI-QEP estimated reaction heats. Combined

UBI-QEP and BEP is a feasible method to rapidly generate surface reaction energetics, which could be used as input parameters of microkinetic model and efficiently aid the computational catalyst prediction.

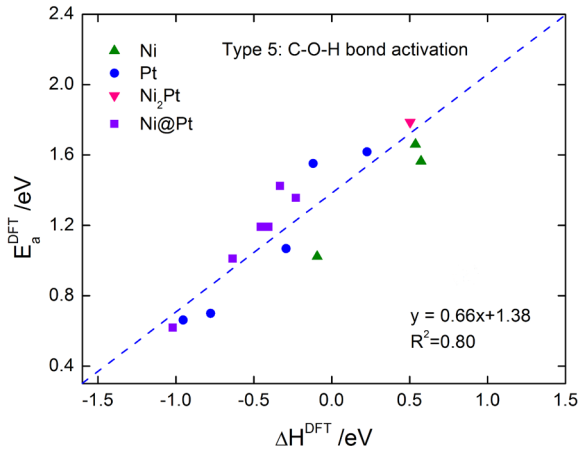

Fig. S1. BEP relationship for C-O-H type reactions, fitted by DFT calculated values.

In this work, all energies are converted to 'generalized formation energies' with respect to gas phase H_2, H_2O and CH_4. At first, the gas phase total energies of H_2, H_2O and CH_4 are calculated by DFT computations, defined as U_{H2}, U_{H2O}, and U_{CH4}, respectively. By using these energies as reference, the energy of one H, C and O atom can be estimated by $R_H = 0.5U_{H2}$; $R_C = U_{CH4} - 4R_H$; $R_O = U_{H2O} - 2R_H$. Then the formation energies are calculated from total energy of isolated species (U_{AB}), adsorption energy ($-Q_{AB}$), activation energy (ΔE) and R_C, R_O and R_H.

For intermediates, the formation energy of $C_xH_yO_z$ is estimated by $E_{CxHyOz} = U_{CxHyOz} - Q_{CxHyOz} - xR_C - yR_H - zR_O$.

For reaction AB* ↔ A_B* ↔ A* + B*, the formation energy of A_B (transition state) is estimated by $E_{A\_B} = E_{AB} + \Delta E_{forward}$ or $E_{A\_B} = E_A + E_B + \Delta E_{reverse}$, where E_{AB}, E_A, E_B are formation energies of AB, A and B, respectively; $\Delta E_{forward}$ and $\Delta E_{reverse}$ are forward and reverse activation energies, respectively.

Table S1. Modeling predicted net turnover frequency (TOF_{Net}^{Cal}, s^{-1}) for elementary steps involved in the microkinetic model over Ni(111), Ni(100) and Ni(211) surfaces at 773 K

No.	Elementary steps	Ni(111)	Ni(100)	Ni(211)
(1)	H_2O (g) + * ↔ H_2O*	2.49 × 10^{-4}	1.06 × 10^{-1}	5.83 × 10^{-1}
(2)	H_2O* + * ↔ H* + OH*	2.49 × 10^{-4}	1.05 × 10^{-1}	5.83 × 10^{-1}
(3)	OH* + * ↔ O* + H*	2.42 × 10^{-4}	9.53 × 10^{-2}	5.53 × 10^{-1}
(4)	CH_4 (g) + 2* ↔ CH_3* + H*	2.49 × 10^{-4}	1.06 × 10^{-1}	5.83 × 10^{-1}
(5)	CH_3* + * ↔ CH_2* + H*	2.49 × 10^{-4}	1.06 × 10^{-1}	5.83 × 10^{-1}
(6)	CH_2* + * ↔ CH* + H*	2.49 × 10^{-4}	1.07 × 10^{-1}	5.83 × 10^{-1}
(7)	CH* + * ↔ C* + H*	7.40 × 10^{-6}	1.01 × 10^{-2}	3.04 × 10^{-2}
(8)	CH_4 (g) + OH* + * ↔ CH_3* + H_2O*	2.00 × 10^{-11}	-3.66 × 10^{-10}	3.50 × 10^{-9}
(9)	CH_4 (g) + O* + * ↔ CH_3* + OH*	4.21 × 10^{-8}	1.77 × 10^{-9}	7.30 × 10^{-5}
(10)	CH_3* + OH* ↔ CH_2* + H_2O*	5.47 × 10^{-11}	-1.36 × 10^{-8}	4.10 × 10^{-9}
(11)	CH_3* + O* ↔ CH_2* + OH*	2.88 × 10^{-8}	-1.92 × 10^{-8}	1.69 × 10^{-5}
(12)	CH_2* + OH* ↔ CH* + H_2O*	4.82 × 10^{-12}	-4.04 × 10^{-4}	-1.07 × 10^{-7}
(13)	CH_2* + O* ↔ CH* + OH*	2.14 × 10^{-9}	-4.81 × 10^{-4}	4.47 × 10^{-6}
(14)	C* + OH* ↔ COH* + *	7.07 × 10^{-6}	1.00 × 10^{-2}	3.01 × 10^{-2}
(15)	COH* + * ↔ CO* + H*	7.14 × 10^{-6}	1.01 × 10^{-2}	3.02 × 10^{-2}
(16)	C* + O* ↔ CO* + *	3.29 × 10^{-7}	3.53 × 10^{-5}	2.86 × 10^{-4}
(17)	CH* + O* ↔ HCO* + *	2.42 × 10^{-4}	9.57 × 10^{-2}	5.53 × 10^{-1}
(18)	HCO* + * ↔ CO* + H*	2.42 × 10^{-4}	9.57 × 10^{-2}	5.53 × 10^{-1}
(19)	CH* + OH* ↔ HCOH* + *	6.52 × 10^{-8}	3.18 × 10^{-5}	1.29 × 10^{-4}
(20)	HCOH* + * ↔ HCO* + H*	2.77 × 10^{-11}	1.22 × 10^{-9}	8.08 × 10^{-9}
(21)	HCOH* + * H* + COH*	6.52 × 10^{-8}	3.18 × 10^{-5}	1.29 × 10^{-4}
(22)	CO* ↔ CO (g) + *	2.49 × 10^{-4}	1.06 × 10^{-1}	5.83 × 10^{-1}
(23)	H* + H* ↔ H_2 (g) + 2*	7.48 × 10^{-4}	3.17 × 10^{-1}	1.75 × 10^{0}
(24)	COH* + O* ↔ COOH* + *	3.65 × 10^{-9}	9.37 × 10^{-9}	5.36 × 10^{-5}
(25)	CO* + OH* ↔ COOH* + *	-3.63 × 10^{-9}	-9.35 × 10^{-9}	-5.35 × 10^{-5}
(26)	COOH* + * ↔ CO_2 (g) + H* + *	1.88 × 10^{-11}	2.01 × 10^{-11}	1.59 × 10^{-7}

Table S2. Experimental measured activation energy, entropy change and pre-exponential factor on Ni catalysts towards different particle size (773 – 848 K, S/C=3.5, CH_4/H_2=1.0, 1 bar)

Catalyst	d_{Ni} [nm]	Activation energy [kJ/mol]	Entropy change [J/(mol·K)]	Pre-exponential factor [$s^{-1}kPa^{-1}$]
12Ni-HT_2	8.3	112.6	-126.8	4.04E+06
12Ni-HT_4	10.2	92.0	-153.2	1.68E+05
12Ni-HT_3	11.3	103.6	-139.7	8.48E+05
12Ni-HT_1	12	101.8	-142.1	6.42E+05

Table S3. DFT calculated C and O formation energies on Ni(111), Ni(211) and Ni(100) surfaces. The energies are reference to gas phase H_2, H_2O and CH_4

Metals	C formation energy (eV)			O formation energy (eV)		
	M(111)	M(211)	M(100)	M(111)	M(211)	M(100)
Ni	2.28	1.32	1.00	0.06	-0.18	-0.31

Table S4. Ni Surface fractions with respect to Ni particle size, based on a truncated octahedron model [8]

Ni particle size/nm	Ni Surface fraction		
	Ni(111)	Ni(100)	Ni(211)
1.3	0.459	0.049	0.492
2.6	0.614	0.112	0.274
3.6	0.685	0.110	0.205
4.9	0.715	0.131	0.153
6.2	0.733	0.145	0.122
7.5	0.745	0.154	0.102
8.4	0.762	0.148	0.090
9.8	0.767	0.154	0.079
11.1	0.771	0.159	0.069
12.4	0.774	0.164	0.062
13.3	0.783	0.159	0.058
14.6	0.785	0.162	0.053
16.0	0.786	0.165	0.049

Table S5. The values of RDS transition state free energy (G_{HTS}), microkinetic model predicted main surface species coverage and vacancy coverage (θ_*), as well as forward CH_4 conversion rate (TOF_{CH4}^{Cal}) over Ni(111), Ni(100) and Ni(211) surfaces at 798 K and 823 K

Ni surfaces	798 K			823 K		
	Ni(111)	Ni(100)	Ni(211)	Ni(111)	Ni(100)	Ni(211)
G_{HTS}/eV	2.51	1.46	1.65	2.53	1.49	1.68
θ_{C*}	2.67E-08	0.697	2.36E-04	4.66E-08	0.747	3.10E-04
θ_{CH*}	5.84E-09	0.284	8.12E-05	8.18E-09	0.240	8.45E-05
θ_{O*}	0.186	6.35E-05	0.828	0.183	2.35E-05	0.812
θ_{H*}	0.027	0.011	0.051	0.024	0.006	0.049
θ_*	0.784	0.009	0.112	0.790	0.006	0.132
TOF_{CH4}^{Cal}/s^{-1}	0.045	0.135	1.398	0.079	0.094	2.669

References

[1] E. Shustorovich, Surf. Sci. Rep. 6 (1986) 1-63.
[2] E. Shustorovich, Acc. Chem. Res. 21 (1988) 183-189.
[3] E. Shustorovich, H. Sellers, Surf. Sci. Rep. 31 (1998) 1-119.
[4] Y. Wang, L. Xiao, Y. Qi, M. Mahmoodinia, X. Feng, J. Yang, Y. Zhu, D. Chen, (Submitted).
[5] E. Shustorovich, A. V. Zeigarnik, Surf. Sci. 527 (2003) 137-148.
[6] E. M. Shustorovich, A. V. Zeigarnik, Russ. J. Phys. Chem. 80 (2006) 4-30.
[7] E. Shustorovich, Russ. J. Phys. Chem. B 1 (2007) 307-329.
[8] D. W. Blaylock, Y. A. Zhu, W. H. Green, Top. Catal. 54 (2011) 828.